



Cite this: *RSC Adv.*, 2023, **13**, 21225

Glowing selenates: novel alkaline earth nanoparticles†

Natalie Kuhlmann  and Claudia Wickleder*

Up to now, no selenate nanoparticles have been described even though much research has been done on respective oxidic compounds such as sulfates and phosphates. For the first time, alkaline earth selenates of the composition $MSeO_4$ ($M = Ca, Sr, Ba$) were synthesized as nanoparticles or nanorods as described in this publication. For this purpose, a micro emulsion method was applied using CTAB as a surfactant. Using X-ray diffraction measurements (XRD) phase purity of the materials could be proven. Furthermore, the nanoparticles were analyzed by raster electron microscopy (REM) and dynamic light scattering (DLS) measurements. Finally, the products were doped with small amounts of Eu^{3+} to obtain luminescent materials. Successful doping was demonstrated by luminescence investigations in the region of 18 000 to 14 000 cm^{-1} (550–715 nm). Incorporation of Eu^{3+} led to strong red-emitting nanoparticles. Low temperature measurements at 10 K allowed conclusions about the site symmetry of Eu^{3+} ions located on the alkaline earth sites.

Received 14th March 2023
Accepted 15th June 2023

DOI: 10.1039/d3ra01669b

rsc.li/rsc-advances

Introduction

Inorganic phosphors have gained a strong interest in bulk form or, above all, as nanomaterials. Possible applications of these phosphors are display applications, LEDs, upconversion materials or nano-thermometry.^{1–3} However, the fundamental understanding of the optical properties is still being examined for many systems, and the development of novel luminescent materials is necessary as well. Furthermore, most of the applications require materials in nano-sized form (*e.g.* bioimaging⁴ or luminescent inks⁵) while others are at least more effective by using nanocrystallites (like luminescent films or coatings^{1,6}).

For many rare earth doped materials, the luminescent properties are described in the literature. The trivalent rare earth elements, especially Eu^{3+} , Sm^{3+} or Tb^{3+} , are suitable in this context due to their large stability against air and humidity and also due to their long-time stability also at higher temperatures using appropriate host lattices. Trivalent rare earth elements show narrow emission bands at typical positions independently from the host lattice.⁷ Eu^{3+} is the most prominent among them with its red to orange emission color. It emits radiation in the range of about 590 to 700 nm.⁸ The intensity of the emission bands itself depends on the site symmetry of the rare earth ion in the host lattice.⁹

Altogether, the luminescence properties of Eu^{3+} ions are well understood. Publications of Eu^{3+} in manifold systems, like

halides,¹⁰ oxides^{1,11} or silicates¹² are already available. Also Eu^{3+} -doped complex oxidic host lattices like sulfates,^{13,14} phosphates^{15,16} and aluminates^{4,11} are known in both, bulk and nanocrystalline form. Also less prominent crystal classes like arsenates or vanadates are already described as host lattices for Eu^{3+} .^{17–19} However, up to now, no selenate compounds are presented as host lattices for any rare earth ion. The reason for this may be the fact that selenates decompose already at moderate temperatures. Therefore, common solid state synthesis as well as melting synthesis for corresponding bulk materials is not possible.

Here, we present rare earth doped alkaline earth selenates, $MSeO_4$ ($M = Ca, Sr, Ba$), for the first time together with an investigation of the luminescence properties of $SrSeO_4:Eu^{3+}$. For this goal, we used micro emulsion techniques below 100 °C to obtain respective materials as nanoparticles as well as in nanorod forms. Beside the novelty of the materials in general, also the nanosize of the particles must be highlighted, which allows the additional use for several applications, like bioimaging.

Materials and methods

Materials

For the preparation of the doped alkaline earth-selenate nanoparticles micro emulsion technique was used. In detail, 1-octadecene (ODC, technical grade, 90%, Alfa Aesar) was used as oil phase together with cetyltrimethylammonium bromide (CTAB, purity 98%, Alfa Aesar) and 1-hexanol (purity > 95%, J. T. Baker) as surfactant and co-surfactant. Distilled water and ethanol (technical grade, ChemSolute) were used without

Department of Chemistry, University of Siegen, 57068 Siegen, Germany. E-mail: wickleder@chemie.uni-siegen.de

† Electronic supplementary information (ESI) available. See DOI: <https://doi.org/10.1039/d3ra01669b>



further purification. The reactants sodium selenate (purity $\geq 98\%$, Alfa Aesar), barium chloride ($\text{BaCl}_2 \cdot 2\text{H}_2\text{O}$, $\geq 99.0\%$, Merck), calcium chloride ($\text{CaCl}_2 \cdot 2\text{H}_2\text{O}$, practical grade, Merck), and strontium chloride ($\text{SrCl}_2 \cdot 6\text{H}_2\text{O}$, practical grade, Fischer Chemical) were used as purchased. $\text{EuCl}_3 \cdot 6\text{H}_2\text{O}$ was prepared from Eu_2O_3 (99.99%, smart elements) by dissolving in HCl (analytical grade, Fischer Scientific) and evaporating the acid. The resulting powders were analysed by X-ray diffraction measurements.

Preparation of selenate nanoparticles

A water-in-oil (w/o) micro emulsion was used for the synthesis of the alkaline earth nanoparticles.²⁰ For this purpose, ODC (50 ml) was mixed with the surfactants CTAB (3 g) and 1-hexanol (5 ml). After the addition of the aqueous phase (Na_2SeO_4 in 0.5 ml distilled water), a stable and transparent micro emulsion could be obtained. The corresponding alkaline earth chloride and europium chloride dissolved in 2.5 M HCl (1 ml) were added dropwise at 60 °C. Precipitation of a colourless product starts immediately. The calculated amount of product was 0.2 g and the molar ratio of alkaline earth ions to SeO_4^{2-} ions was 1.1 : 1. A small excess of alkaline earth ions was used to ensure a complete precipitation of selenate ions. For doped samples 2 mol% of MCl_2 were replaced by EuCl_3 .

In case of doped samples, a high temperature micro emulsion synthesis (HT-ME) was additionally performed by adding the following steps to the synthesis procedure above: after the precipitation took place, the micro emulsion was heated to 120 °C to evaporate the volatile compounds and afterwards stirred at 200 °C under reflux for 2 h. This step increases the crystallinity of the products, and, thus, improves the luminescence intensity.²¹ Finally, the mixture was allowed to cool down below 50 °C. The precipitate was collected by centrifugation and washed with water and ethanol several times in all cases. Drying of particles was done in a compartment dryer at 80 °C.

Characterization methods

Sample composition and phase purity of all samples were checked with a HUBER G 21 X-ray diffractometer using a $\text{Cu-K}_{\alpha 1}$ (0.154056 nm) radiation. Afterwards, the results were compared to theoretical XRD patterns collected from the Inorganic Crystal Structure Database (ICSD).

Furthermore, particle sizes were determined by dynamic light scattering (DLS) measurements using a ZETASISER NANO ZS from MALVERN PANANLYTICAL equipped with a He-Ne-Laser ($\lambda = 633$ nm). For the measurement, the samples are dispersed in diethylene glycol (viscosity 35.7 cP) and treaded with an ultrasonic beam. The measurement took place at 20 °C. The intensity of the backscattered light was measured at an angle of 173°. For size calculation the refraction indices of the samples are required. They were calculated according to the ionic refractions of the elements in each sample.²² Namely, 1.5847 for $\text{CaSeO}_4 \cdot 2\text{H}_2\text{O}$, 1.7249 for SrSeO_4 and 1.7717 for BaSeO_4 were employed.

Images of selected selenate nanoparticles were recorded with a QUANTA FEG 250 raster electron microscope equipped with a large field detector in low vacuum mode.

Luminescence properties of the doped samples were examined with a FLUOROLOG-3 FL3-22 spectrometer from HORIBA JOBIN YVON equipped with a 450 W xenon arc lamp. Emission was detected with a HAMAMATSU photomultiplier tube R928P (equipped with an additional Ulbricht sphere for photoluminescence quantum yield (PLQY) measurements). The recorded emission spectra were corrected for the photomultiplier sensitivity. For the determination of the PLQY the excitation and emission of each sample doped with 2 mol% Eu^{3+} were measured in a range of 370–420 nm resp. 550–725 nm alternating with a BaSO_4 standard in triplicate and an average value was calculated from the three measurements.

Results and discussion

MSeO_4 and $\text{MSeO}_4 \cdot \text{Eu}^{3+}$ nanoparticles were successful synthesized for the first time. Fig. 1 depicts results of XRD of SrSeO_4 measurements compared to reference patterns out of the ICSD. In detail, it shows doped and undoped SrSeO_4 with comparison to its reference.²³ Even though, the intensity ratio of the nanoparticles in the range of 25 to 30° is different from that of the reference, the samples without thermal treatment (undoped and “ME”) may be described as phase pure materials. The intensity differences can be explained by preferred orientations during crystallization of nanoparticles. The position of the reflections itself agrees with the reference. The reflection around 20° marked with a * can be explained as an artifact from the used foil during the sample preparation. Doping of 2 mol% Eu^{3+} seems not to have an impact on the final crystal structure as it can be seen in Fig. 1. Consequently, the introduced charge (replacing M^{2+} with Eu^{3+}) must be balanced. This can be compensated by oxygen on interstitial sites as well as alkaline

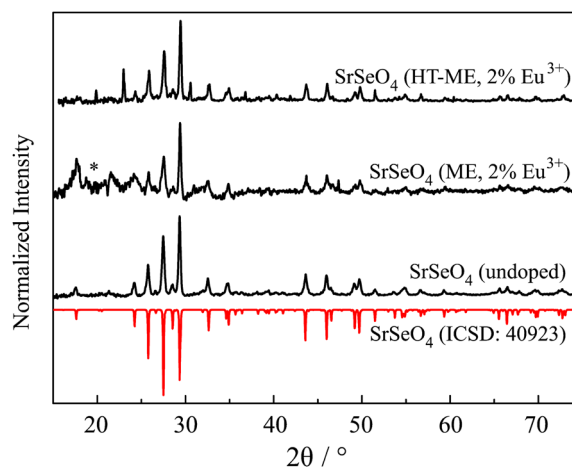


Fig. 1 XRD pattern of SrSeO_4 compared to the theoretical pattern abstracted from ICSD.²³ Results of undoped SrSeO_4 and doped with 2 mol% Eu^{3+} using micro emulsion synthesis (ME) and after thermal treatment at 200 °C (HT-ME). Reflection marked with * can be assigned to an artifact of the measurement.



earth vacancies. Especially for nanoparticles (which have a relatively high surface area), the introduced charges can be balanced by surface defects and a charged particle surface. In this case, the surface would be positively charged, which is compensated by the adhesion of the negatively charged CTAB ions.

The reflections of the two doped Sr samples are slightly shifted to higher 2θ values. An inset of Fig. 1 is shown in the ESI S1.† This is an indication that Eu^{3+} is successfully incorporated into the host lattice. Shorter bond distances (due to a smaller ionic radius of Eu^{3+})²⁴ lead to a shift to larger 2θ .²⁵ Unfortunately, the doped sample with thermal treatment (HT-ME) shows two reflections originated by Na_2SeO_4 (at 24 and 31°). It can be assumed that this was not indicated by the higher temperature itself. Decomposition of selenates at high temperatures would rather lead to selenite ions as observed for the Ca sample. Thus, it can be assumed that SrSeO_4 can be prepared and stabilized using CTAB at 200°C . The impurification of Na_2SeO_4 seems not to have an influence on the optical properties of the sample. Both doped samples show the same behavior at low temperature with respect to their Stark-splitting. In case of doping on the Na layer in Na_2SeO_4 , a deviating behavior must be observed here at the latest.⁹ In addition, doping onto the Sr layer is preferred over Na^+ in terms of charge, ion size and coordination number.²⁴ Furthermore, the HT-ME sample has a better signal-to-noise ratio compared to the same product without the thermal treatment at 200°C . This implies the higher crystallinity after the “*in situ*-sintering step” which might enhance the PLQY and might be advantageous for other applications.

XRD results of undoped BaSeO_4 and $\text{CaSeO}_4 \cdot 2\text{H}_2\text{O}$ compared to the theoretical pattern^{26,27} are depicted in Fig. 2. The same behavior as in case of the heat-treated doped sample of SrSeO_4 could be observed for BaSeO_4 . Unfortunately, $\text{CaSeO}_4 \cdot 2\text{H}_2\text{O}$ already starts to decompose during the HT-ME step at 200°C . Hence, the doped sample of $\text{CaSeO}_4 \cdot 2\text{H}_2\text{O}$ was synthesized as the undoped one without the *in situ*-sintering step.

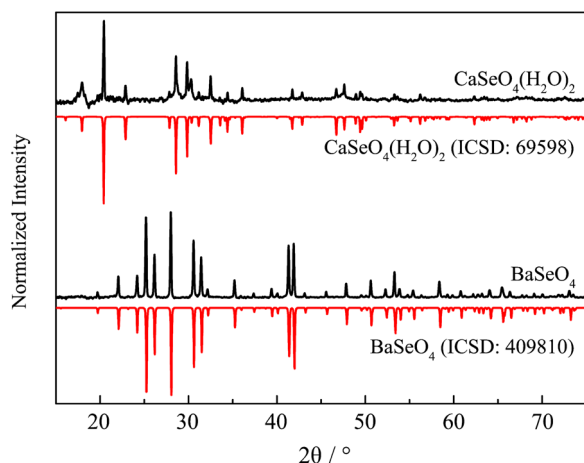


Fig. 2 XRD pattern of BaSeO_4 and $\text{CaSeO}_4 \cdot 2\text{H}_2\text{O}$ compared to the theoretical pattern abstracted from ICSD.^{24,25}

XRD patterns of the doped Ba and Ca selenates are shown in the ESI S2 and S3.† The XRD patterns presented above (Fig. 1 and 2) were used to calculate the particle size with the aid of the Scherrer equation.²⁸ For this purpose, the experimental FWHM of the three most intense reflections between 20 and 35° was used according to eqn (1). The average calculated size of the particles is depicted in Table 1.

$$\tau = \frac{K\lambda}{\beta \cos \theta} \quad (1)$$

In the equation, τ is the mean size of the domains, K is a dimensionless shape factor, here set as 1, λ is the X-ray wavelength (0.154056 nm), θ is the Bragg angle and β is the line broadening at FWHM, after subtracting the instrumental line broadening, in radians. Reflection of SiO_2 at 27° was used to calculate the instrumental line broadening for the region from 20 to 35° .

The samples were additionally analyzed using DLS measurements to determine the particle size of the dispersed NPs. The respective results are shown in Fig. 3 and summarized in Table 1. A comparison of undoped SrSeO_4 prepared at 60°C and the doped out of HT-ME synthesis proves that the thermal treatment does not lead to particle growth or agglomeration. This behavior can be explained by a CTAB shell on the NPs surface, that avoids agglomeration at higher temperatures. This has also been described for syntheses of other nanomaterials from the same microemulsion.²¹ The calculated particle size (Scherrer) and measured size distribution (by DLS) is similar in both cases (Fig. 3a and b). However, DLS measurements seem to depict that the particles are polydisperse. Especially for SrSeO_4 and CaSeO_4 two main sizes of the particles (around 40 nm and 200 to 1000 nm) are indicated.

Interestingly, REM images of selenate NPs depict rod-like shape for the Ca and fiber-shape for the Sr compound, while spherical particles for BaSeO_4 were observed, as shown in Fig. 4. This is in agreement with the DLS investigations (only one size determined for the Ba compound). Thus, the observations of two size distributions of $\text{CaSeO}_4 \cdot 2\text{H}_2\text{O}$ and SrSeO_4 (Fig. 3) can be explained by the particle morphology (smaller size as diameter and larger size as length of the rods/fibers). The proportion of smaller and larger sizes (respectively diameter and length) seems to depend on the compound itself, but not on the synthesis method or sample preparation for the measurements. While the percentage ratio between the two size distributions is around 20% (diameter) to 80% (length) for

Table 1 Particle size of selected selenate nanoparticles derived from DLS measurements and calculated according to the Scherrer equation

Compound		Particle size/nm	
		DLS	Scherrer
$\text{CaSeO}_4 \cdot 2\text{H}_2\text{O}$		38 (50%), 321 (50%)	48 ± 2
SrSeO_4	Undoped	35 (20%), 439 (80%)	31 ± 4
	2% Eu^{3+}	43 (20%), 518 (80%)	29 ± 9
	HT-ME	36 (25%), 287 (80%)	35 ± 6
BaSeO_4		55	54 ± 11

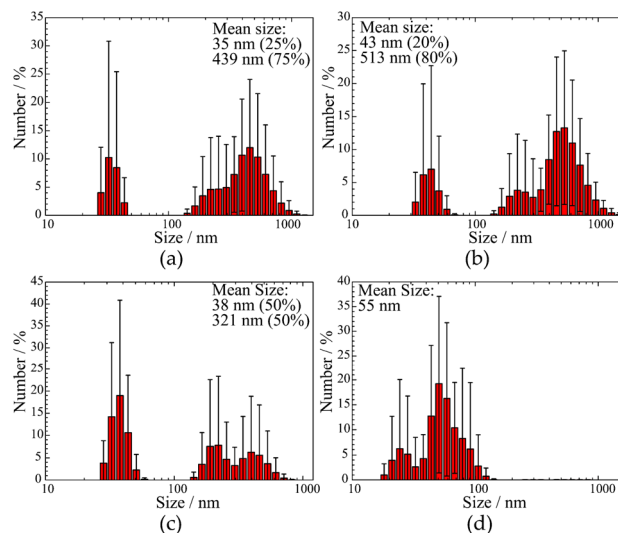


Fig. 3 Size determination of selenate nanoparticles determined by DLS measurements. (a) Undoped SrSeO_4 , (b) $\text{SrSeO}_4:\text{Eu}^{3+}$ (2%) after temperature treatment at 200 °C, (c) undoped CaSeO_4 , (d) undoped BaSeO_4 . Percentage values in (a), (b), and (c) reflect the proportion of the size distribution of the total peak area.

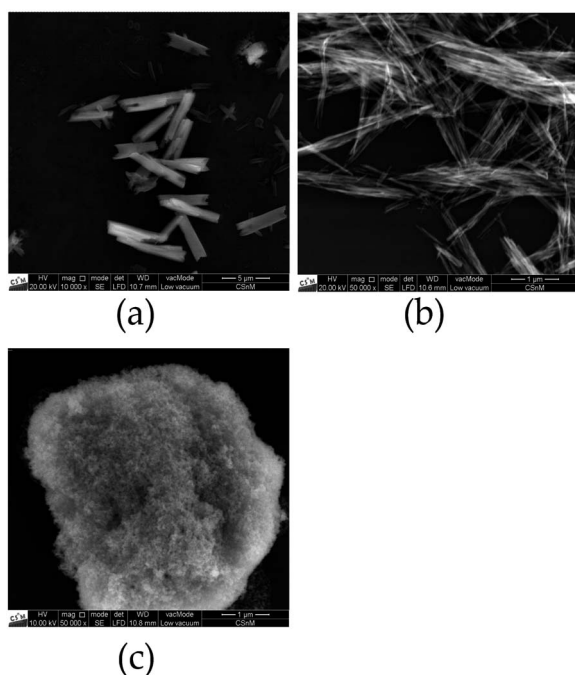


Fig. 4 REM images of doped MSeO_4 samples in a low vacuum mode, detected with a large field detector and magnification of $1\text{--}5 \times 10^4$ the corresponding scales are shown in the lower right corner of each REM photograph. (a) $\text{CaSeO}_4 \cdot 2\text{H}_2\text{O}$, (b) SrSeO_4 , (c) BaSeO_4 .

SrSeO_4 (resulting in nano-fibers) in several DLS measurements and different batches, it is around 50% to 50% for the Ca samples (resulting in nano-rods), as it can be seen in Fig. 3a–c and 4a, b. The REM image of BaSeO_4 shows large agglomerates while the individual small particles/spheres are still visible. A

common feature of the Ca and Sr compound is that both crystallize in a monoclinic crystal system, while BaSeO_4 is orthorhombic. It is known that minerals of monoclinic systems can grow preferentially in one room direction, such as in gypsum crystals. This occurs less frequently in orthorhombic. Systems. This crystallization behavior could explain the different shape of BaSeO_4 compared to the Sr and Ca compound.

In summary, the calculated particle sizes are similar for all samples whether determined by the Scherrer equation or by DLS (regarding the smaller determined size, if two different sizes are found), although the Stokes–Einstein equation (DLS) assumes spherical particles and determines a hydrodynamic radius²⁹ plus there is no suitable shape factor for cylindrical NPs with the diameter to length ratio shown in REM (Scherrer).³⁰ One has to take these points into account as it comes to a comparison between the size calculation with the Scherrer equation or with DLS. Fortunately, in this case, both calculated values are in a good agreement. A second larger diameter between 430 and 520 nm could be additionally determined by DLS measurements for Ca and Sr compounds. This can be explained with the rod-like or fiber shape, respectively, for $\text{CaSeO}_4 \cdot 2\text{H}_2\text{O}$ and SrSeO_4 . The length of the rods can be determined to 1 to 5 μm by REM measurements for most of the particles. The size difference to roughly 0.5 μm length (determined by DLS) can be explained by a better dispersion medium and dispersion time for the DLS measurements and sedimentation of large particles in an aqueous medium.

Finally, the optical properties of the selenate NPs were investigated. The corresponding emission spectra are depicted in Fig. 5. On the left side, room temperature emission spectra of the Ca, Sr and Ba selenate NPs are compared. All materials show typical Eu^{3+} emission peaks arising from the $4f\text{--}4f$ transitions with a maximum around 615 nm (assigned to $^5\text{D}_0 \rightarrow ^7\text{F}_2$ transitions). Due to different host lattices and, thus, coordination numbers and bond lengths, the ratio of the emission peaks varies. However, the stark splitting seems to be nearly identical in all cases.

According to the crystal structure of the host lattices and assuming doping on the alkaline earth site, a C_1 site symmetry is expected for the Eu^{3+} ion in all samples. The emission spectrum of $\text{SrSeO}_4:\text{Eu}^{3+}$ recorded at 10 K is shown in Fig. 5b

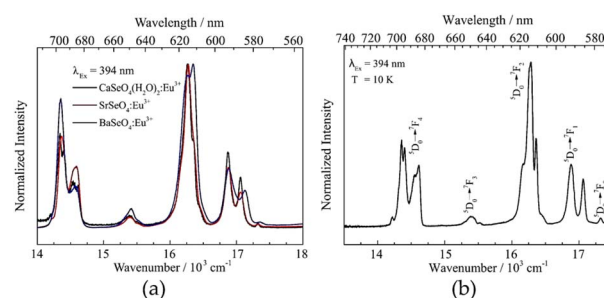


Fig. 5 Emission spectra of $\text{MSeO}_4:\text{Eu}^{3+}$ (2%) NPs excited at 394 nm. (a) Room temperature spectra of $\text{M} = \text{Ca}, \text{Sr}, \text{and Ba}$, (b) fine splitting of $\text{SrSeO}_4:\text{Eu}^{3+}$ observed at 10 K with assignments of transitions starting from $^5\text{D}_0$ excited state into the different ground states $^7\text{F}_j$.



exemplarily. Here, the fine splitting can be observed more in detail due to lower occupation of higher states. Although the resolution is certainly lower compared to bulk (crystalline) samples. The optical transitions are assigned by the Dieke-diagram,³¹ while the number of stark levels for each transition depends on the site symmetry of the Eu^{3+} ion.⁹ Due to a relatively large surface area in nanomaterials the site symmetry of the doped ions may vary between ions located on the surface and those in the core. Therefore, the exact number of stark levels (of Eu^{3+} ions in the core, assumed C_1 symmetry) could not be determined, even at 10 K. However, the presence of a $^5\text{D}_0 \rightarrow ^7\text{F}_0$ transition implies that Eu^{3+} occupies a C_{nv} , C_n or C_s site.³² Furthermore, at least two stark levels for the $^5\text{D}_0 \rightarrow ^7\text{F}_1$ transition and at least four for the $^5\text{D}_0 \rightarrow ^7\text{F}_2$ transition could be observed. This confirms a low site symmetry (like C_1) and, thus, the successful incorporation of Eu^{3+} (in addition to the observed shift observed in the XRD pattern, cf. in the ESI S1†) in the host lattice onto the alkaline earth site. Similar observations are made in other monazite compounds like $\text{LaPO}_4:\text{Eu}^{3+}$.^{15,33} The excitation spectra of the Ca, Sr, and Ba compound recorded at an emission wavelength of 615 nm are shown in the ESI S4.† The PLQY of $\text{MSeO}_4:\text{Eu}^{3+}$ (2%) compounds were determined as well. SrSeO_4 has a PLQY of 14% while the Ca compound showed a PLQY of 8%. $\text{BaSeO}_4:\text{Eu}^{3+}$ has with 6% the lowest PLQY among them. This can be explained by the slight yellow coloration of the sample. Here, more relaxation processes will occur due to defect levels, which leads to the lower PLQY. The obtained PLQY can be compared quite well with other published data of oxidic nanomaterials. Eu_2O_3 on a SiO_2 substrate, for example, achieves a PLQY of about 10%.³⁴ A higher PLQY (above 30%) was found in sodium zinc molybdate nanomaterials by codoping with Li^+ ions.³⁵ However, it is also shown that the PLQY scales with the particle size. In case of $\text{Gd}_2\text{O}_3:\text{Eu}^{3+}$ NPs the PLQY decreases from 23% (135 nm) to 4% (15 nm).³⁶ Our particles might experience further quenching due to the organic CTAB shell. Therefore, the quantum yield of the first described light emitting selenate (nano)particles is with around 10% very encouraging.

Conclusions

Selenate nanoparticles were successfully synthesized for the first time. In detail, alkaline earth nanoparticles of the composition MSeO_4 ($\text{M} = \text{Sr}, \text{Ba}$) and $\text{CaSeO}_4 \cdot 2\text{H}_2\text{O}$ were synthesized using a w/o micro emulsion with the aid of CTAB and 1-octadecene. Different *in situ*-sintering steps and heating procedures led to similar size distributions around 50 nm. DLS and REM investigations were performed to examine the morphology of the NPs, the respective results are in agreement with those calculated by XRD measurements. Ba selenate NPs had a spherical shape, while Ca has a rod-like-, and Sr a fiber-shape with a length of about 500 nm (DLS). Larger particles or agglomerates were found by dispersing the products in ethanol instead of diethylene glycol. Here, the length of the rods was up to 5 μm with still a small diameter (REM). Furthermore, all nanoparticles could be doped with Eu^{3+} to get glowing selenate NPs for the first time with a PLQY around 10%. Emission spectra

depict peaks typical for Eu^{3+} ions with maxima at about 613 nm. A low site symmetry of the Eu^{3+} ion doped in SrSeO_4 could be confirmed by emission measurements at 10 K. The amount of Stark levels for the $^5\text{D}_0 \rightarrow ^7\text{F}_j$ ($j = 0-4$) indicated a low site symmetry, which is in agreement to C_1 in SrSeO_4 .

Author contributions

N. Kuhlmann wrote the complete draft of this manuscript. She did the synthetic work, all measurements as well as the interpretation and conclusion of the results. Prof. Dr C. Wickleder gave the input to this project, supervised and discussed it and optimized the manuscript to its final form.

Conflicts of interest

There are no conflicts to declare.

Acknowledgements

The authors acknowledge Dr Christian Pritzel, University of Siegen, for the SEM measurements.

References

- 1 R.-S. Liu and X.-J. Wang, *Phosphor Handbook: Novel Phosphor, Synthesis, and Applications*, CRC Press, Boca Raton, 3rd edn, 2021.
- 2 Y. H. Kim, N. S. M. Viswanath, S. Unithrattil, H. J. Kim and W. B. Im, *ECS J. Solid State Sci. Technol.*, 2017, 7, R3134.
- 3 C. D. S. Brites, P. P. Lima, N. J. O. Silva, A. Millán, V. S. Amaral, F. Palacio and L. D. Carlos, *Nanoscale*, 2012, 4, 4799.
- 4 R.-S. Liu and X.-J. Wang, *Phosphor Handbook: Experimental Methods for Phosphor Evaluation and Characterization*, CRC Press, Boca Raton, 3rd edn, 2021.
- 5 Y. Liu, D. Tu, H. Zhu and X. Chen, *Chem. Soc. Rev.*, 2013, 42, 6924–6958.
- 6 H. Terraschke and C. Wickleder, *Chem. Rev.*, 2015, 115, 11352–11378.
- 7 *Phosphor handbook*, ed. W. M. Yen, S. Shionoya and H. Yamamoto, CRC Press/Taylor and Francis, Boca Raton, FL, 2nd edn, 2007.
- 8 G. Blasse and B. C. Grabmaier, *Luminescent materials*, Springer-Verlag, Berlin, New York, 1994.
- 9 K. Binnemans, *Coord. Chem. Rev.*, 2015, 295, 1–45.
- 10 Q. Ju, Y. Liu, R. Li, L. Liu, W. Luo and X. Chen, *J. Phys. Chem. C*, 2009, 113, 2309–2315.
- 11 G. Blasse, *J. Chem. Phys.*, 1966, 45, 2356–2360.
- 12 H. C. Streit, J. Kramer, M. Suta and C. Wickleder, *Materials*, 2013, 6, 3079–3093.
- 13 D. Van Der Voort and G. Blasse, *J. Solid State Chem.*, 1990, 87, 350–359.
- 14 B. Zhai, D. Liu, Y. He, L. Yang and Y. M. Huang, *J. Lumin.*, 2018, 194, 485–493.
- 15 S. K. Gupta, P. S. Ghosh, M. Sahu, K. Bhattacharyya, R. Tewari and V. Natarajan, *RSC Adv.*, 2015, 5, 58832–58842.



- 16 B. V. Ratnam, M. K. Sahu, A. K. Vishwakarma, K. Jha, H.-J. Woo, K. Jang and M. Jayasimhadri, *J. Lumin.*, 2017, **185**, 99–105.
- 17 L. Benarafa, L. Rghiou, S. Zaydoun, M. Idrissi, A. Lorriaux and F. Wallart, *Phys. Chem. News*, 2009, **49**, 111–119.
- 18 A. Lorriaux-Rubbens, E. Antic-Fidancev, M. Lemaitre-Blaise, P. Porcher and F. Wallart, *J. Alloys Compd.*, 1998, **275–277**, 412–415.
- 19 A. Strzep, A. Watras, K. Zawisza, P. Boutinaud and R. J. Wiglus, *Inorg. Chem.*, 2017, **56**, 10914–10925.
- 20 S. Wolf and C. Feldmann, *Angew. Chem., Int. Ed.*, 2016, **55**, 15728–15752.
- 21 D. H. M. Buchold and C. Feldmann, *Adv. Funct. Mater.*, 2008, **18**, 1002–1011.
- 22 A. S. Korotkov and V. V. Atuchin, *Opt. Commun.*, 2008, **281**, 2132–2138.
- 23 H. Prévost-Czeskleba and H. Endres, *Acta Crystallogr., Sect. C: Struct. Chem.*, 1984, **40**, 18–20.
- 24 R. D. Shannon, *Acta Crystallogr., Sect. A: Cryst. Phys., Diffraction, Theor. Gen. Crystallogr.*, 1976, **32**, 751–767.
- 25 F. Kang, Y. Hu, L. Chen, X. Wang, H. Wu and Z. Mu, *J. Lumin.*, 2013, **135**, 113–119.
- 26 A. Andara, M. A. Salvado, Á. Fernández-González, S. García-Granda and M. Prieto, *Z. Kristallogr. - New Cryst. Struct.*, 2005, **220**, 5–6.
- 27 R. R. Krüger and W. Abriel, *Acta Crystallogr., Sect. C: Struct. Chem.*, 1991, **47**, 1958–1959.
- 28 P. Scherrer and P. Debye, *Nachr. Ges. Wiss. Goettingen, Geschaefliche Mitt.*, 1918, **1918**, 98–100.
- 29 C. C. Miller, *Proc. R. Soc. Lond., Ser. A Contain. Pap. Math. Phys. Character*, 1924, **106**, 724–749.
- 30 S. Lele and T. R. Anantharam, *Proc. - Indian Acad. Sci., Sect. A*, 1966, **64**, 261–274.
- 31 G. H. Dieke, *Spectra and energy levels of rare earth ions in crystals*, Wiley, New York, 1968.
- 32 T. Gavrilović, K. Laganovska, A. Zolotarjovs, K. Smits, D. J. Jovanović and M. D. Dramićanin, *Opt. Mater.*, 2018, **82**, 39–46.
- 33 J. Dexpert-Ghys, R. Mauricot and M. D. Faucher, *J. Lumin.*, 1996, **69**, 203–215.
- 34 G. Bellocchi, G. Franzò, F. Iacona, S. Boninelli, M. Miritello, T. Cesca and F. Priolo, *Opt. Express*, 2012, **20**, 5501–5507.
- 35 N. Jain, R. Paroha, R. K. Singh, S. K. Mishra, S. K. Chaurasiya, R. A. Singh and J. Singh, *Sci. Rep.*, 2019, **9**, 2472.
- 36 C. Liu, J. Liu and K. Dou, *J. Phys. Chem. B*, 2006, **110**, 20277–20281.

